



Structural Basis for Selective Oxidation of Phosphorylated Ethylphenols by Cytochrome P450 Monooxygenase CreJ

Sheng Dong,^{a,i} Jingfei Chen,^{a,i} Xingwang Zhang,^b Fei Guo,^b Li Ma,^b Cai You,^b Xiao Wang,^c Wei Zhang,^{b,g} Xiaobo Wan,^{a,d}
 Shuang-Jiang Liu,^{e,i} Li-Shan Yao,^{a,i} Shengying Li,^{b,h} Lei Du,^{a,b,f}  Yingang Feng^{a,i}

^aShandong Provincial Key Laboratory of Synthetic Biology, CAS Key Laboratory of Biofuels, Qingdao Institute of Bioenergy and Bioprocess Technology, Chinese Academy of Sciences, Qingdao, Shandong, China

^bState Key Laboratory of Microbial Technology, Shandong University, Qingdao, Shandong, China

^cQingdao Industrial Energy Storage Research Institute, Qingdao Institute of Bioenergy and Bioprocess Technology, Chinese Academy of Sciences, Qingdao, China

^dLaboratory of Optoelectronic Chemical Materials and Devices, Ministry of Education, School of Chemical & Environmental Engineering, Jiangnan University, Wuhan, China

^eState Key Laboratory of Microbial Resources, and Environmental Microbiology and Biotechnology Research Center at Institute of Microbiology, Chinese Academy of Sciences, Beijing, China

^fShenzhen Branch, Guangdong Laboratory for Lingnan Modern Agriculture, Genome Analysis Laboratory of the Ministry of Agriculture, Agricultural Genomics Institute at Shenzhen, Chinese Academy of Agricultural Sciences, Shenzhen, China

^gThe State Key Laboratory of Bio-organic and Natural Products Chemistry, Chinese Academy of Sciences, Shanghai, China

^hLaboratory for Marine Biology and Biotechnology, Qingdao National Laboratory for Marine Science and Technology, Qingdao, Shandong, China

ⁱUniversity of Chinese Academy of Sciences, Beijing, China

Sheng Dong and Jingfei Chen contributed equally to this work. The order of their names was agreed upon by both authors.

ABSTRACT Selective oxidation of C-H bonds in alkylphenols holds great significance for not only structural derivatization in pharma- and biomanufacturing but also biological degradation of these toxic chemicals in environmental protection. A unique chemomimetic biocatalytic system using enzymes from a *p*-cresol biodegradation pathway has recently been developed. As the central biocatalyst, the cytochrome P450 monooxygenase CreJ oxidizes diverse *p*- and *m*-alkylphenol phosphates with perfect stereoselectivity at different efficiencies. However, the mechanism of regio- and stereoselectivity of this chemomimetic biocatalytic system remained unclear. Here, using *p*- and *m*-ethylphenol substrates, we elucidate the CreJ-catalyzed key steps for selective oxidations. The crystal structure of CreJ in complex with *m*-ethylphenol phosphate was solved and compared with its complex structure with *p*-ethylphenol phosphate isomer. The results indicate that the conformational changes of substrate-binding residues are slight, while the substrate promiscuity is achieved mainly by the available space in the catalytic cavity. Moreover, the catalytic preferences of regio- and stereoselective hydroxylation for the two ethylphenol substrates is explored by molecular dynamics simulations. The ethyl groups in the complexes display different flexibilities, and the distances of the active oxygen to H_{pro-S} and H_{pro-R} of methylene agree with the experimental stereoselectivity. The regioselectivity can be explained by the distances and bond dissociation energy. These results provide not only the mechanistic insights into CreJ regio- and stereoselectivity but also the structural basis for further P450 enzyme design and engineering.

IMPORTANCE The key cytochrome P450 monooxygenase CreJ showed excellent regio- and stereoselectivity in the oxidation of various alkylphenol substrates. C-H bond functionalization of these toxic alkylphenols holds great significance for both biological degradation of these environmental chemicals and production of value-added structural derivatives in pharmaceutical and biochemical industries. Our results, combined with *in vitro* enzymatic assays, crystal structure determination of enzyme-substrate complex, and molecular dynamics simulations, provide not only

Citation Dong S, Chen J, Zhang X, Guo F, Ma L, You C, Wang X, Zhang W, Wan X, Liu S-J, Yao L-S, Li S, Du L, Feng Y. 2021. Structural basis for selective oxidation of phosphorylated ethylphenols by cytochrome P450 monooxygenase CreJ. *Appl Environ Microbiol* 87:e00018-21. <https://doi.org/10.1128/AEM.00018-21>.

Editor Robert M. Kelly, North Carolina State University

Copyright © 2021 American Society for Microbiology. All Rights Reserved.

Address correspondence to Lei Du, dulei@qibebt.ac.cn, or Yingang Feng, fengyg@qibebt.ac.cn.

Received 5 January 2021

Accepted 4 March 2021

Accepted manuscript posted online 12 March 2021

Published 11 May 2021

significant mechanism elucidation of the regio- and stereoselective catalyzation mediated by CreJ but also the promising directions for future engineering efforts of this enzyme toward more useful products. It also has great extendable potential to couple this multifunctional P450 enzyme with other biocatalysts (e.g., hydroxyl-based glycosylase) to access more alkylphenol-derived high-value chemicals through environment-friendly biocatalysis and biotransformation.

KEYWORDS cytochrome P450 monooxygenase, ethylphenol, selective oxidation, crystal structure, molecular dynamics

Cytochrome P450 monooxygenases (CYPs), which are believed to be the most versatile biocatalysts in nature (1, 2), constitute a superfamily of heme-containing enzymes that are widely distributed among all kingdoms of life (3–5). This family of enzymes can recognize a wide variety of substrates and catalyze regio- and stereospecific reactions, showing diverse mechanisms of substrate binding and oxidative catalysis (6–8). A prerequisite for tailoring specific functions for P450 applications is to understand the structure-activity relationship between the target molecule and the enzyme (9).

Recently, we engineered a unique chemomimetic bio-oxidation system for the functionalization of aliphatic C-H bonds in alkylphenols, containing protection/direction, oxidation, and deprotection steps, which is originated from the *p*-cresol biodegradation pathway in the Gram-positive bacterium *Corynebacterium glutamicum* (Fig. 1) (10, 11). As the central biocatalyst, the P450 enzyme CreJ (CYP288A2) (12) is able to accept a broad range of phosphorylated *para*- and *meta*-alkylated phenols as the substrates and to catalyze successive oxidations with different efficiencies. Thus, CreJ provides a valuable example of P450 enzymes with native substrate promiscuity, which is essential for protein design and engineering (13). However, the mechanism of CreJ recognizing different *p*- and *m*-substituted substrates has not been fully elucidated. Understanding the mechanism will be helpful for efficiency improvement and selectivity control of CreJ toward any substrate of interest.

Our previous studies demonstrated that the methylene groups at the benzyl position of *p*- and *m*-ethylphenol phosphates were completely oxidized in a stereoselective manner with an *S* configuration exclusively established (11). The crystal structures of CreJ in complex with the *p*-ethylphenol phosphate showed that the *pro-S* hydrogen atom in the methylene group is closer to the heme-iron reactive center than the *pro-R* hydrogen atom, which well explained the stereoselectivity (11). However, the mechanism of the perfect stereoselectivity of CreJ toward *m*-ethylphenol phosphate remains unknown. More importantly, the distances of the aliphatic C-H bonds to the active oxygen atom are critical for regioselectivity, stereoselectivity, and catalytic activity, but the active oxygen atom was not observed in the crystal structures of CreJ in its ferric status. Furthermore, our previous studies showed that the phosphorylated *m*-ethylphenol was converted with a significantly lower conversion ratio than that of phosphorylated *p*-ethylphenol (11), which cannot be explained merely using the structure of CreJ-*p*-ethylphenol phosphate complex.

In this study, we focused on the catalytic characteristics of CreJ to elucidate the mechanism of its substrate promiscuity, catalytic efficiency, regioselectivity, and stereoselectivity by directly using phosphorylated *p*- and *m*-ethylphenol substrates. The crystal structure of CreJ in complex with *m*-ethylphenol phosphate was solved and compared with the previous structure of CreJ-*p*-ethylphenol phosphate complex. Molecular dynamics simulations were performed to further illustrate the mechanical difference when CreJ reacts with the two isomeric substrates. The enzymatic characteristics, crystal structures, and molecular dynamics simulations reported here provide new insights into the substrate specificity and catalytic mechanism of CreJ, which paves the way for enzyme engineering and application of these ethylphenols.

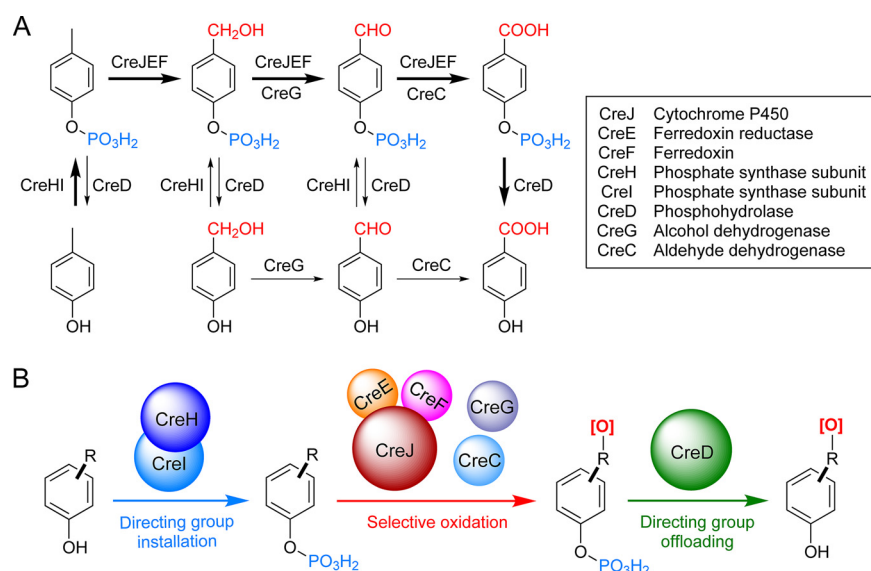


FIG 1 The *p*-cresol biodegradation pathway in *Corynebacterium glutamicum* (A) and the developed chemomimetic bio-oxidation system for *p*- and *m*-substituted alkylphenols (B). Bold arrows indicate the major metabolic pathway mediated by P450 CreJ.

RESULTS

Selective oxidation of phosphorylated *p*- and *m*-ethylphenols by P450 CreJ. To precisely identify the characteristics of the central catalyst CreJ, we synthesized the two substrates of CreJ, namely, *p*- and *m*-ethylphenol phosphates (1 and 2), which were used to skip the phosphorylation step catalyzed by CreHI in the previously mixed-enzyme assays (Fig. 1). To overcome the challenges of purifying the phosphorylated products with high polarity, the phosphohydrolase CreD was subsequently added into the reactions to remove the phosphate group, and the dephosphorylated products were readily identified.

With phosphate 1 as the substrate, besides the previously reported three oxidized/hydrolyzed products 1'a, 1'b, and 1'c (with 83.6% yield of 1'a as the predominated product) (11), an additional new product with the retention time of 17.1 min was also detected (Fig. 2A). Based on high-resolution mass spectrometry (HRMS) (Fig. S1 in the supplemental material) and a comparison with the authentic standard, it was determined to be *p*-vinylphenol (product 1'd). When phosphate 2 was used as a substrate, four oxidative products (2'a, 2'b, 2'c, and 2'd) were detected (Fig. 2B), similar to the product pattern in the previous study (11). Chiral high-performance liquid chromatography (HPLC) analysis based on the retention time comparison with the authentic enantiomer standards showed that pure enantiomer *S*-1'a and *S*-2'a products (enantiomeric excess [ee] > 99%) were also obtained when we directly used the two phosphorylated ethylphenols. The desaturated products 1'd and 2'd in these enzyme assays are likely attributed to the direct desaturation of the ethyl group, as reported in other P450 enzymes (14). There were also unoxidized products, 1' and 2', generated from dephosphorylation of the unreacted substrates by CreD (Fig. 2). All the oxidized products and unreacted substrates were dephosphorylated, indicating that CreD has high hydrolyzing activities toward different phosphorylated alkylphenols. The conversion ratio of the oxidation step catalyzed by CreJ became lower with alkylphenol substrates larger than *p*- or *m*-cresol, indicating that the CreJ-mediated oxidation steps played a significant role for efficient oxidations of these ethylphenolic substrates.

To elucidate the reason for the lowered efficiency, spectroscopic substrate-binding assays were performed to determine the substrate-binding affinities of CreJ toward substrates 1 and 2 (Fig. 3). The equilibrium dissociation constants (K_D) for CreJ with

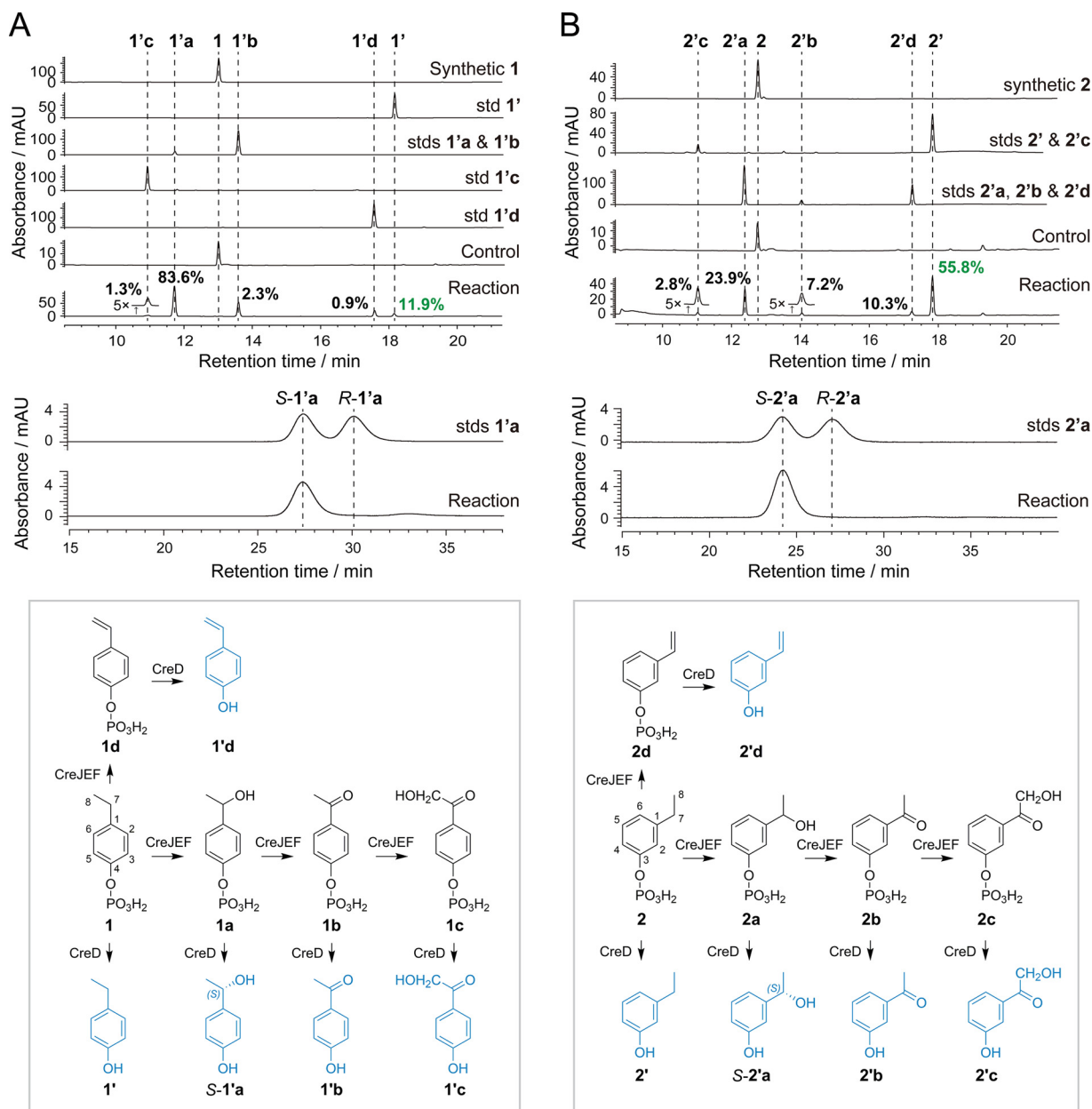


FIG 2 HPLC analyses (top), stereochemistry determination (middle), and catalytic schemes (bottom) of the reactions using *p*-ethylphenol phosphate (phosphate 1) (A) and *m*-ethylphenol phosphate (phosphate 1) (B) as the substrates. Substrate concentration in enzymatic reactions and controls was 1 mM. std(s), standard(s). The percentage numbers in black indicate the yield (conversion ratio) of the specific product. The percentage numbers in green represent the ratio of the unreacted substrate. Due to distinct extinction coefficients, the peak intensities of compounds do not necessarily reflect relative amounts shown as percentages.

substrates 1 and 2 were determined to be 0.09 mM and 0.15 mM, respectively, both of which were greater than that (0.06 mM) of *p*-methylphenol phosphate (i.e., phosphorylated *p*-cresol). These results indicate that the affinities of substrates 1 and 2 are lower than that of *p*-methylphenol phosphate. The order of the substrate-binding affinities is consistent with the order of the conversion ratios, suggesting the binding affinity could be one of the major reasons for CreJ's activity.

Structure of CreJ in complex with *m*-ethylphenol phosphate. Previously, we determined the structure of CreJ in complex with *p*-ethylphenol phosphate (CreJ-1, PDB ID 5XJN). To further elucidate the mechanism of substrate promiscuity and catalytic stereoselectivity of CreJ, the crystal structure of CreJ in complex with *m*-

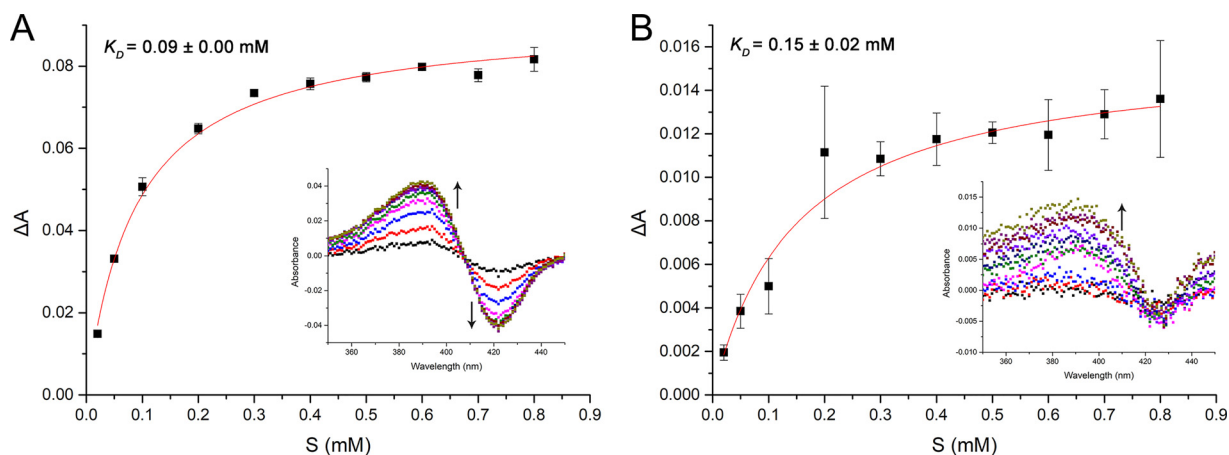


FIG 3 Substrate binding curves of 1 (A) and 2 (B) to CreJ. $\Delta A = A_{390\text{ nm}} - A_{420\text{ nm}}$; S represents the total substrate concentration. Arrows indicate the increase of ligand concentration.

ethylphenol phosphate (CreJ-2; PDB ID 7CCF) was solved in this study. The structure had a resolution of 2.80 Å, and the data collection and refinement statistics are listed in Table S1. The crystals of CreJ-2 belong to the $P4_32_12$ space group, and there is one molecule in each asymmetric unit, which is the same as the CreJ-1 complex (11). Substrate 2 was observed with unambiguous electron densities located in the substrate-binding cavity of CreJ similar to that of substrate 1 (Fig. 4) (11). In brief, the polar phosphate moiety of substrate 2 is fixed by residues Q83 and S106 to S109 from the B₂C loop and R194 and S261 via hydrogen bonds or electrostatic interactions. Furthermore, the non-polar part of substrate 2 is recognized mostly by aromatic residues, including W199, F264, W315, and F416, making the ethyl terminus of substrate 2 adjacent to the heme iron. The distance between the *pro-S* hydrogen atom of the methylene group and the heme iron is 3.6 Å, significantly closer than that of the *pro-R* hydrogen atom (4.7 Å) (Fig. 4F), indicating the *pro-S* hydrogen has many more chances to be oxidized, which is consistent with the enzymatic results of exclusively generating the *S* configuration product.

Structural comparison of CreJ in complex with *m*- and *p*-ethylphenol phosphates. With the crystal structures of CreJ-1 (11) and CreJ-2, we can analyze the structure-activity relationship of CreJ in more detail. The overall structures of CreJ in the two complexes are almost the same (with a C α root mean square deviation [RMSD] of 0.179 Å), except for small differences in some flexible regions (Fig. 4B). Furthermore, the critical residues responsible for substrate recognition have only slight conformational differences in the two structures (Fig. 4C). However, the benzene rings of substrates 1 and 2 showed a significant shift (~ 0.7 Å) away from the heme (Fig. 4C). Interestingly, this shift makes the phosphate groups and the ethyl groups of the two substrates be in similar positions, resulting in similar substrate anchoring by the phosphate groups and the catalytic possibility for their ethyl groups at different positions (Fig. 4C and D). Because the residues surrounding the substrate benzene ring have no significant conformational changes, the shifted benzene ring in the CreJ-2 structure mainly occupies the available space in the catalytic cavity with reduced distances to surrounding residues (Fig. 4G and H). These results suggest that the substrate promiscuity of CreJ mainly depends on the available space of the substrate-binding cavity. Therefore, the future engineering of CreJ for substrate spectrum expansion could be focused on the modification of the cavity space and shape.

In the crystal structures, the methylene carbon (C-7) of substrates 1 or 2 is farther than the terminal methyl carbon (C-8) to the central Fe atom of heme (Fig. 4E and F). However, catalytic reactions showed that CreJ preferentially oxidizes C-7, generating predominated hydroxylated products 1a and 2a (Fig. 2). One possible reason is that the C-H bond dissociation energy of C-7 is much lower than that of C-8 (85.4 and

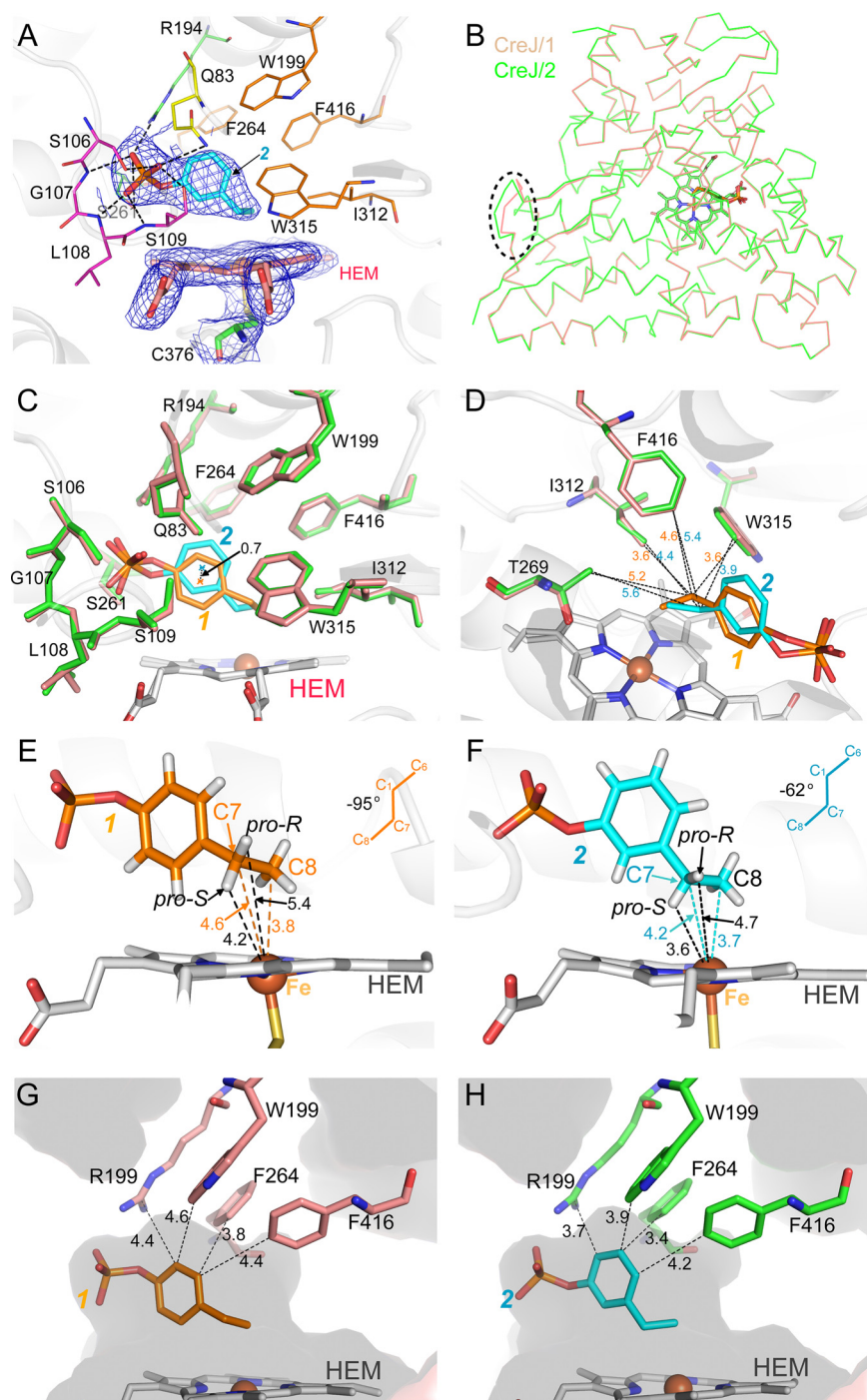


FIG 4 Structural analysis of CreJ in complex with *m*-ethylphenol phosphate (phosphate 2). (A) Structure of the substrate and the surrounding region. Substrate 2 is in cyan; the residues responsible for phosphate 2 recognition are shown by thin sticks. The $2F_oF_c$ densities for 2, heme, and C376 are contoured in blue in 1.0σ . Hydrogen bonds between the enzyme and the phosphate group of 2 are shown as dashed lines. (B) Overlaid backbone ribbons of the CreJ-2 (green) and the CreJ-1 (orange) complexes. The only major conformational difference in a loop region is circled by a dashed ellipse. (C) Comparison of the two substrates (1 and 2) and substrate-binding residues in the two complexes. (D) Comparison of the distances between the substrate C-7 atom and substrate-binding residues in the two complexes. (E) Distances between the ethyl group of 1 and the heme-iron reactive center. (F) Distances between the ethyl group of 2 and the Fe atom of heme. (G and H) The substrate-binding cavity and the distances between the benzene ring and surrounding residues in the structure of CreJ in complex with substrates 1 (G) and 2 (H).

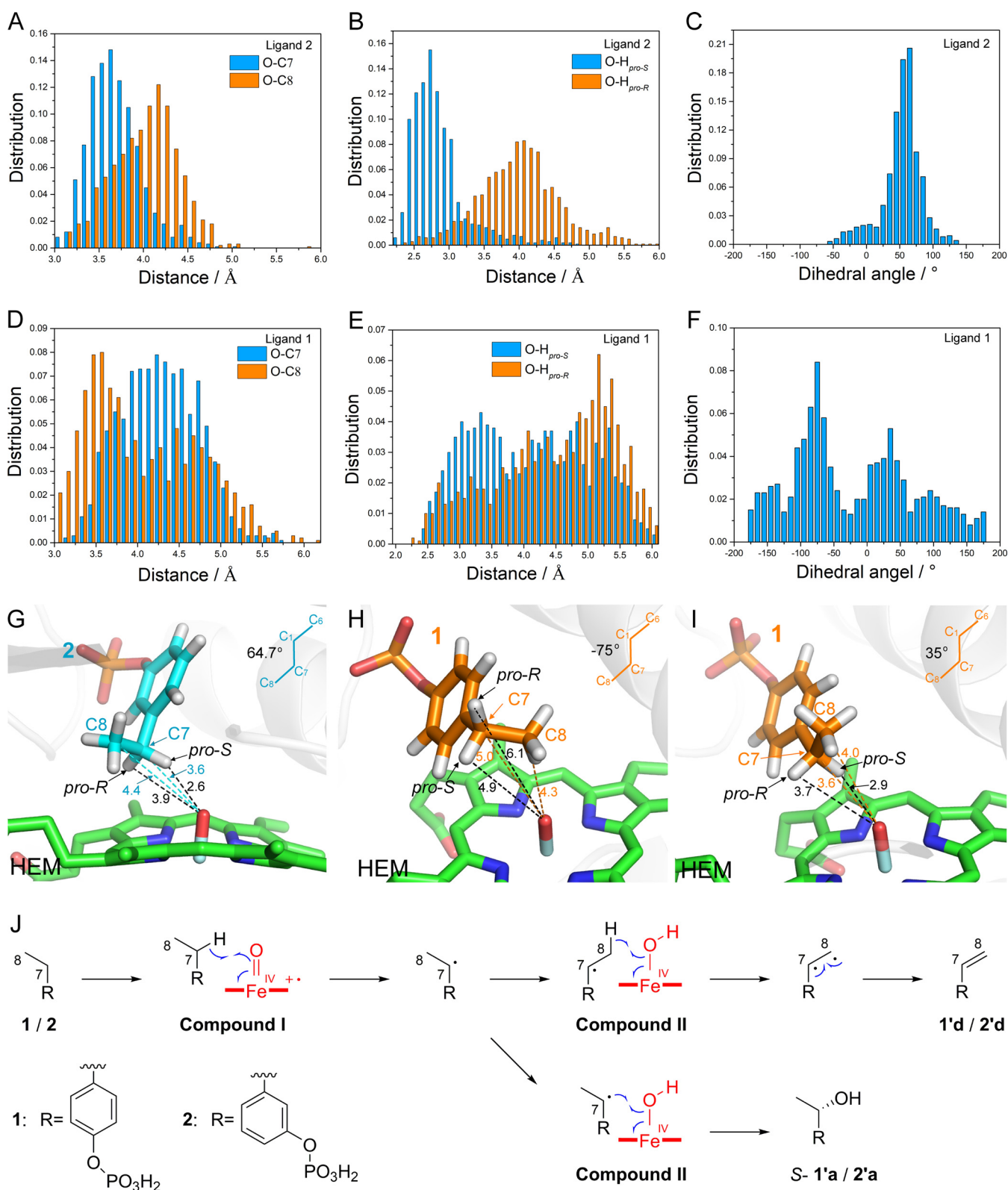


FIG 5 Molecular dynamic simulations analysis using compound 1 of Fe(IV)=O active state (A to I) and proposed catalytic mechanism for hydroxylation and desaturation (J). Probability distributions of the distance between the active oxygen and the adjacent carbon atoms (A and D), methylene hydrogen atoms (B and E), and the dihedral angles (C and F) for ligands 2 and 1, respectively. The most probable conformations for ligand 2 (G) and 1 (H and I) in MD simulations.

100.9 kcal/mol, respectively, reported for ethylbenzene) (15, 16), which might play a critical role in regioselective hydroxylation. The hydroxylation on the C-7 position generated only *S* configuration products, which can be explained by the structures in which the distance between the *pro-S* hydrogen atom of the methylene group and the heme iron is much smaller than that of the *pro-R* hydrogen atom for both substrates 1 and 2 (Fig. 4E and F).

Molecular dynamics simulations-assisted analysis of the regio- and stereoselective mechanism. CreJ-1 and CreJ-2 are both ferric complexes since no dioxygen was observed on the heme iron in both crystal structures. Because compound I (oxyferryl intermediate) in a P450 catalytic cycle (14, 17) is critical to the regio- and stereoselectivity and the substrate-binding cavity has additional space for a certain movement, we performed two molecular dynamics (MD) simulations for the CreJ-1 and CreJ-2 complexes using the widely accepted compound I model in Fe(IV)=O active state (18, 19) to investigate the conformational changes of substrates, thereby elucidating the catalytic regio- and stereoselective preferences.

The results showed that both ligands 1 and 2 have conformational changes because of the existence of active oxygen (O). For ligand 2, the terminal methyl flipped from one side of the benzene ring to the other, and the dihedral angle of C-8-C-7-C-1-C-6 changed from the original -62° to a narrow range distribution with the most probability of 64.7° (Fig. 4F; Fig. 5C and G). This flipping resulted in that the C-8-O distance (a distribution with a peak at 4.2 Å) is larger than the C-7-O distance (a distribution with a peak at 3.7 Å) with a high statistical significance (*t* test, $P < 0.001$) (Fig. 5A), indicating that atom C-7 has more chances to be hydroxylated in addition to the lower C-H bond dissociation energy of C-7. Moreover, the distances O-H_{*pro-S*} and O-H_{*pro-R*} distributed in a range with peaks at 2.7 and 4.1 Å ($P < 0.001$), respectively (Fig. 5B), which supports the formation of the *S* configuration in the experimental assays.

For ligand 1, the methyl can move to both sides of the benzene ring, and the C-8-C-7-C-1-C-6 dihedral angles distribute from -180° to 180° , with the two major peaks at -75° and 35° (Fig. 5F, H, and I). This suggests that the methyl of ligand 1 can rotate about the C7-C1 axis more freely than that of ligand 2. As a result, the C-7-O distance was distributed in a broad range from 3.0 Å to 5.5 Å with a peak at ~ 4.2 Å (Fig. 5D). The C-8-O distance was distributed in a similar range but with the two peaks at 3.5 Å and 4.5 Å (Fig. 5D). Therefore, unlike ligand 2, the regioselectivity of ligand 1 is not dominated by the distances between the carbon atoms and the active oxygen atom. In this case, the lower C-H bond dissociation energy of C-7 might be the major reason for the regioselectivity (15). The distance distribution between active O and atoms H_{*pro-S*}/H_{*pro-R*} also showed a broad range between 2.5 Å to 6.0 Å, but the peak distance of O-H_{*pro-S*} (3.3 Å) is much shorter than that of O-H_{*pro-R*} (5.1 Å) ($P < 0.001$) (Fig. 5E). For the conformations with the two peak dihedral angles (-75° and 35°), the O-H_{*pro-S*} distances (4.9 Å and 2.9 Å) are always shorter than the O-H_{*pro-R*} distances (6.1 Å and 3.7 Å) (Fig. 5H and I). These results also support the *S* configuration selectivity of the reaction with ligand 1 as the substrate.

Direct desaturations were observed for substrates 1 and 2. We hypothesize that the desaturation is most likely the result of a competing pathway following the benzylic radical intermediate, which is formed from initial hydrogen atom abstraction by compound I (Fig. 5J). The hydroxy group is transferred to the benzylic radical intermediate to form hydroxylated products, or the terminal methyl group undergoes a second hydrogen atom abstraction to form desaturated products through diradical intermediates. Similar mechanisms were previously proposed from the oxidation process of duclauxin intermediate by DuxD (20) and ethyl carbamate by CYP2E1 (21). The results of molecular dynamics simulations also show there is sufficient flexibility of the ethyl group to permit the terminal methyl to approach the oxygen atom, which supports the desaturated mechanism to a certain extent.

DISCUSSION

The lower efficiency of CreJ for nonnative substrates is likely related to their lower

binding affinities, as the substrate with lower binding affinity also has a lower conversion ratio. However, besides the binding affinity, multiple factors could affect the catalytic efficiency, such as the bond dissociation energy, the position and angle of the bond to be oxidized, and substrate conformational dynamics. The C-H bond dissociation energy for the methyl of methylbenzene is 88.5 kcal/mol, which is slightly higher than that of C-7 (85.4 kcal/mol) in ethylbenzene (15, 16), but the conversion ratio of *p*-methylphenol phosphate is higher than that of *p*- and *m*-ethylphenol phosphate substrates. In the crystal structures, the methyl carbon atom of *p*-methylphenol phosphate and C-7 carbon atoms of substrates 1 and 2 are located in the distances of 4.7, 4.6, and 4.2 Å to the heme iron, respectively, which suggests that the distance to the catalytic center is not the only reason for the different catalytic efficiencies. Our MD simulations indicate that the ethyl group of substrate 1 has more flexibility than that of substrate 2. Considering the multiple intermediates in the P450 catalytic cycle, this dynamic feature, or the relatively large space around the catalytic center (like the case of *p*-methylphenol phosphate), might be necessary for the intermediate formation and interconversion. If this is true, future engineering for enhancing the catalytic efficiency of CreJ for the nonnative substrates should be focused on the enlargement of the substrate-binding cavity and the increase of the binding affinity.

The TP450 compound I of the Fe(IV)=O active state is more widely accepted by researchers in recent studies and reviews (18, 19, 22), but we cannot exclude the possibility of Fe(IV)-O \cdot active state (23–25) in CreJ compound I. To evaluate this, we further performed MD calculations using Fe(IV)-O \cdot active state. Results showed, for ligand 2, the distance distributions of the active oxygen to C-7/C-8 and H_{pro-S}/H_{pro-R} have a very similar pattern to that of Fe(IV)=O active state, which agrees with the experimental *S* stereoselectivity (Fig. S2). However, for ligand 1, MD results show the opposite *R* configuration dominates the hydroxy product (Fig. S2 in the supplemental material), which disagrees with the enzymatic experiments, reflecting that distance of Fe and active oxygen in compound I active state of CreJ has a significant effect on chiral selectivity of this substrate. These MD results support a Fe(IV)=O active state of compound I for CreJ.

Direct desaturations have been reported in some P450 enzymes, and several P450 enzymes were reported to produce mainly or only desaturated products (14). Although the desaturation products generated by CreJ are minor relative to the alcohols, this P450 enzyme exhibits catalytic promiscuity with the ability of both hydroxylation and desaturation in addition to its excellent substrate compatibility. Considering that the mechanism of desaturation by P450 enzymes is still not very clear, CreJ might be a very good candidate to study the issue.

Taken together, using the synthesized phosphorylated *p*- and *m*-ethylphenols as the substrates, we elucidate the CreJ-catalyzed key steps for selective oxidations. The enzymatic, structural, and simulated results in this study provide not only significant mechanism insights into the regio- and stereoselective oxidations mediated by CreJ but also promising directions for the future engineering efforts for CreJ toward more useful products.

MATERIALS AND METHODS

Chemical synthesis of phosphate substrates. Compound 1 (*p*-ethylphenol phosphate) was chemically synthesized according to our previous report (11). For the synthesis of compound 2 (*m*-ethylphenol phosphate), procedures were carried out following the overview scheme in Fig. S3 in the supplemental material. The structures of synthetic compounds were confirmed by HRMS (Fig. S4 and S5) and nuclear magnetic resonance (NMR; Table S2; Fig. S6 and S7).

(i) Synthesis of diethyl (3-ethylphenol) phosphate. To a solution of *m*-ethylphenol (0.61 g, 5 mmol) dissolved in carbon tetrachloride (10 ml), diethyl phosphite (0.77 ml, 6 mmol) was added at 0°C under argon atmosphere. Triethylamine (0.83 ml, 6 mmol) was carefully added dropwise to the mixture using a dropping funnel. The mixture was stirred overnight at room temperature. Water (15 ml) was added, and the organic layer was separated. The organic layer was washed twice with dilute hydrochloric acid (2 × 15 ml), four times with dilute sodium hydroxide solution (4 × 15 ml), and twice with brine (2 × 15 ml) before being dried over anhydrous MgSO₄. The removal of solvent on rotary evaporator gave a crude, which was further purified by silica gel column chromatography using a petroleum ether/ethyl acetate (4/1, vol/vol) mixture to afford diethyl (3-ethylphenol) phosphate (1.23 g). The yield was 95%.

(ii) **Synthesis of *m*-ethylphenol phosphate 2.** Diethyl (3-ethylphenol) phosphate (1.23 g, 4.8 mmol) was dissolved in dry CH_2Cl_2 (30 ml). Then, bromotrimethylsilane (6.3 ml, 48 mmol) was added to the solution, and the mixture was heated to reflux for 18 h under argon atmosphere. The solvent was evaporated, and the residue was dissolved in anhydrous methanol (30 ml). The solution was stirred for 30 min at 40°C. Then, the resulting solution was concentrated to give phosphate 2 (0.91 g). The yield was 94%.

Protein expression and purification. Proteins CreH, CreI, CreJ, CreE, CreF, and CreD were expressed and purified according to the published procedures (11). The concentration of functional P450 was calculated using the extinction coefficient ($\epsilon_{450\text{ nm}-490\text{ nm}}$) of 91,000 $\text{M}^{-1}\cdot\text{cm}^{-1}$. Concentrations of non-P450 enzymes (CreH, CreI, CreE, CreF, and CreD) were determined by the Bradford method using bovine serum albumin (BSA) as the standard (26).

Crystallization, data collection, and structure determination. The CreJ protein ($\sim 15\text{ mg}\cdot\text{ml}^{-1}$) in the buffer (10 mM Tris-HCl, 100 mM NaCl, pH 7.4) was mixed with 10 mM substrate 2 before crystallization. The crystals of the CreJ-2 complex were obtained using commercial high-throughput screening kits (Hampton Research) and the hanging drop vapor diffusion method with 1 μl of the CreJ protein with 1 μl of well solution. The crystals used for X-ray data collection were obtained in 0.2 M lithium chloride and 20% polyethylene glycol 3350 (PEG 3350), pH 6.8. All crystals were cryoprotected by soaking in well solution supplemented with 30% (vol/vol) glycerol for 30 s and then flash-cooled to 100 K in liquid nitrogen. The data were collected at the Shanghai Synchrotron Radiation Facility, Beamline BL18U, in a 100 K nitrogen stream (27). Data indexing, integration, and scaling were conducted using XDS (28). The CreJ structure was determined by molecular replacement using CCP4 program suite (Collaborative Crystallographic Project number 4) and the PDB file 5GWE as a search model (11, 29). Refinement of the structure was performed using the programs Coot and PHENIX (30, 31). All molecular graphics were created using PyMOL (Schrödinger, LLC; <http://www.pymol.org/>).

Enzyme assays. Enzymatic assays were carried out in 100 μl of 50 mM Tris-HCl buffer (pH 8.0) at 30°C. The reaction mixtures contained CreJ, CreE, CreF, 1 mM substrate (1 or 2), and 2 mM NADPH. Each enzyme was adjusted to a final concentration of 10 μM . After incubation at 30°C for 2 h, CreD (10 μM final concentration) and its cofactor Mg^{2+} (20 mM final concentration) were added into the mixtures, followed by another 2 h of incubation.

Substrate-binding assays. Spectroscopic substrate-binding assays were performed by recording absorbance curves from 350 nm to 550 nm on a UV-visible spectrophotometer (Infinite M200 Pro; Tecan) (32). We titrated 1 μM P450 CreJ in 1 ml of 50 mM sodium phosphate solution (pH 7.4) with a 100-mM substrate solution. Data consisting of absorbance differences ΔA ($A_{390\text{ nm}} - A_{420\text{ nm}}$) and corresponding substrate concentrations (ranging from 0.02 to 0.8 mM) were plotted and fitted to the hyperbolic function $\Delta A = A_{\text{max}}S/(K_D + S)$ (S for the total substrate concentration, A_{max} for the maximal absorption shift at saturation, and K_D for the apparent dissociation constant of the enzyme-substrate complex).

Analytical methods for product identification. Three volumes of MeOH were added to quench *in vitro* enzymatic reactions, and the precipitated proteins were removed by centrifugation at the maximum speed for 10 min. Supernatants were analyzed with an Agilent 1260 Infinity high-performance liquid chromatography (HPLC) system (Agilent Technologies, USA) with a photodiode array detector. A Triart C18 column (YMC Co., Ltd., Japan) was used for compounds separation with a linear mobile phase gradient ranging from 2% (vol/vol) acetonitrile in 0.1% (vol/vol) trifluoroacetic acid (TFA) aqueous solution to 80% (vol/vol) acetonitrile in 0.1% (vol/vol) TFA aqueous solution over 30 min. The injection volume was 10 μl , and the flow rate was set to 1 ml/min. The detection wavelength was set to 275 nm. HRMS was recorded in the negative or/and positive ionization mode on an LQC Deca XP Plus ion trap mass spectrometer (Thermo Finnigan, San Jose, CA, USA). Structural assignments of metabolites were performed by comparing the retention time of a detected compound with the corresponding authentic standard, as well as HRMS data. Chiral HPLC analysis was performed according to our previous report (11). The two enantiomers of products 1'a and 2'a were, respectively, separated on a chiral column using an isocratic mobile phase of hexane containing 10% isopropanol over 60 min. The absolute configuration was confirmed by retention time comparison with the enantiomerically pure authentic standards.

Molecular dynamics simulation. The molecular dynamics (MD) simulations were performed with the GROMACS package (33). The initial coordinates of protein and ligands were assigned based on the X-ray crystal structure. The P450 compound I active state was constructed by adding O above the Fe of the heme. Two MD simulations were separately performed using Fe(IV)=O active state and Fe(IV)-O \cdot active state. The distances of Fe-O were set to 1.65 Å and 1.81 Å in P450 compound I of Fe(IV)=O active state (18, 19) and Fe(IV)-O \cdot active state (23, 24), respectively. The protonation states of the phosphate group of the ligand were assigned by PROPKA 3.1 (34) at pH 7.4. CHARMM36 force field and CHARMM general force field (CGenFF) were used for modeling protein and ligand, respectively. The parameters of the heme ring and Fe=O moiety were adopted according to a previous report (35). An isothermal-isobaric (NPT) ensemble was adopted in the initial relaxation of simulation systems. The pressure was controlled to be 1 bar by the Parrinello-Rahman method (36, 37). The temperature was maintained at 300 K by the usage of the Nose-Hoover thermostat (38). The particle-mesh Ewald method (39, 40) was used to evaluate the contributions of the long-range electrostatic interactions. Nonbonded interactions were cut off at 1.2 nm using the Verlet scheme (41) and a force switch at 1.0 nm for the van der Waals modifier. All bonds to hydrogen atoms in the protein were constrained using the LINCS algorithm (42), whereas bonds and angles of water molecules were constrained by the SETTLE algorithm (43). A time step of 2 fs was used. After 500 ps of preequilibrium with protein C α atoms and ligand restrained using positional restraints force constant of 1,000 $\text{kJ mol}^{-1}\cdot\text{nm}^{-2}$, 10 ns of production MD was carried out. The trajectory was saved every 10 ps.

Data availability. Coordinates and associated structure factors have been deposited in Protein Data Bank (PDB) with the PDB ID 7CCF.

SUPPLEMENTAL MATERIAL

Supplemental material is available online only.

SUPPLEMENTAL FILE 1, PDF file, 0.7 MB.

ACKNOWLEDGMENTS

This work was supported by the National Key Research and Development Program of China (2020YFA0907900 and 2019YFA0905100), the Shandong Provincial Natural Science Foundation of China (ZR2020ZD23 and ZR2019BB024 to L.D. and ZR2019ZD20 to S.L.), the National Natural Science Foundation of China (31800041 to L.D., 31700694 to S.D., 32000039 to X.Z., 32071266 to L.M., and 21472204 and 32025001 to S.L.), the State Key Laboratory of Bio-organic and Natural Products Chemistry, CAS (SKLBNPC18242 to W.Z.), the National Postdoctoral Innovative Talents Support Program (BX20180325 to L.D.), QIBEBT and Dalian National Laboratory For Clean Energy (I201925 to S.D. and I201804 to Y.F.), the Director Innovation Foundation of Qingdao Institute of Bioenergy and Bioprocess Technology (to L.-S.Y. and Y.F.), and the Fundamental Research Funds of Shandong University (2019GN030 to L.M.).

S.D., J.C., X. Wan, S.-J.L., L.-S.Y., S.L., L.D., and Y.F. designed this research; F.G. and L.D. performed molecular cloning and enzymatic assays; S.D. carried out crystallographic experiments and structural analysis; C.Y. and L.M. analyzed crystal structures; J.C. performed molecular dynamics simulation and related analysis; X.Z. performed compounds assignment; X. Wang synthesized the substrates; and S.D., J.C., W.Z., X. Wan, S.-J.L., L.-S.Y., S.L., L.D., and Y.F. analyzed the data and prepared the manuscript.

We declare no conflict of interest. This article does not contain any studies with human or animal subjects performed by any of the authors.

REFERENCES

- Coon MJ. 2005. Cytochrome P450: nature's most versatile biological catalyst. *Annu Rev Pharmacol Toxicol* 45:1–25. <https://doi.org/10.1146/annurev.pharmtox.45.120403.100030>.
- Roiban GD, Agudo R, Reetz MT. 2014. Cytochrome P450 catalyzed oxidative hydroxylation of achiral organic compounds with simultaneous creation of two chirality centers in a single C-H activation step. *Angew Chem Int Ed Engl* 53:8659–63. <https://doi.org/10.1002/anie.201310892>.
- Werck-Reichhart D, Feyereisen R. 2000. Cytochromes P450: a success story. *Genome Biol* 1:reviews3003.1. <https://doi.org/10.1186/gb-2000-1-6-reviews3003>.
- Guengerich FP. 2002. Cytochrome P450 enzymes in the generation of commercial products. *Nat Rev Drug Discov* 1:359–366. <https://doi.org/10.1038/nrd792>.
- Podust LM, Sherman DH. 2012. Diversity of P450 enzymes in the biosynthesis of natural products. *Nat Prod Rep* 29:1251–1266. <https://doi.org/10.1039/c2np20020a>.
- Sibbesen O, Zhang Z, Ortiz de Montellano PR. 1998. Cytochrome P450cam substrate specificity: relationship between structure and catalytic oxidation of alkylbenzenes. *Arch Biochem Biophys* 353:285–296. <https://doi.org/10.1006/abbi.1998.0632>.
- Sugimoto H, Shiro Y. 2012. Diversity and substrate specificity in the structures of steroidogenic cytochrome P450 enzymes. *Biol Pharm Bull* 35:818–823. <https://doi.org/10.1248/bpb.35.818>.
- Niwa T, Imagawa Y. 2016. Substrate specificity of human cytochrome P450 (CYP) 2C subfamily and effect of azole antifungal agents on CYP2C8. *J Pharm Sci* 19:423–429. <https://doi.org/10.18433/J31553>.
- Urban P, Lautier T, Pompon D, Truan G. 2018. Ligand access channels in cytochrome P450 enzymes: a review. *Int J Mol Sci* 19:1617. <https://doi.org/10.3390/ijms19061617>.
- Du L, Ma L, Qi F, Zheng X, Jiang C, Li A, Wan X, Liu SJ, Li S. 2016. Characterization of a unique pathway for 4-cresol catabolism initiated by phosphorylation in *Corynebacterium glutamicum*. *J Biol Chem* 291:6583–6594. <https://doi.org/10.1074/jbc.M115.695320>.
- Du L, Dong S, Zhang X, Jiang C, Chen J, Yao L, Wang X, Wan X, Liu X, Wang X, Huang S, Cui Q, Feng Y, Liu SJ, Li S. 2017. Selective oxidation of aliphatic C-H bonds in alkylphenols by a chemomimetic biocatalytic system. *Proc Natl Acad Sci U S A* 114:E5129–E5137. <https://doi.org/10.1073/pnas.1702317114>.
- Nelson DR. 2009. The cytochrome p450 homepage. *Hum Genomics* 4:59–65. <https://doi.org/10.1186/1479-7364-4-1-59>.
- Leveson-Gower RB, Mayer C, Roelfes G. 2019. The importance of catalytic promiscuity for enzyme design and evolution. *Nat Rev Chem* 3:687–705. <https://doi.org/10.1038/s41570-019-0143-x>.
- Guengerich FP. 2018. Mechanisms of cytochrome P450-catalyzed oxidations. *ACS Catal* 8:10964–10976. <https://doi.org/10.1021/acscatal.8b03401>.
- Altarawneh MK, Dlugogorski BZ, Kennedy EM, Mackie JC. 2013. Rate constants for reactions of ethylbenzene with hydroperoxyl radical. *Combust Flame* 160:9–16. <https://doi.org/10.1016/j.combustflame.2012.08.008>.
- Carey FA, Sundberg RJ. 2007. *Advanced organic chemistry. Part a: structure and mechanisms*, 5th ed. Springer Science+Business Media, LLC, New York, NY.
- Ortiz de Montellano PR. 2015. Substrate oxidation by cytochrome P450 enzymes, p 111–176. *In* Ortiz de Montellano PR (ed), *Cytochrome P450: structure, mechanism, and biochemistry*, 4th ed. Springer International Publishing, Cham, Switzerland.
- Petrović D, Bokel A, Allan M, Urlacher VB, Strodel B. 2018. Simulation-guided design of cytochrome P450 for chemo- and regioselective macrocyclic oxidation. *J Chem Inf Model* 58:848–858. <https://doi.org/10.1021/acs.jcim.8b00043>.
- Li Z, Jiang YY, Guengerich FP, Ma L, Li SY, Zhang W. 2020. Engineering cytochrome P450 enzyme systems for biomedical and biotechnological applications. *J Biol Chem* 295:833–849. [https://doi.org/10.1016/S0021-9258\(17\)49939-X](https://doi.org/10.1016/S0021-9258(17)49939-X).
- Gao S-S, Zhang T, Garcia-Borràs M, Hung Y-S, Billingsley JM, Houk KN, Hu Y, Tang Y. 2018. Biosynthesis of heptacyclic duclauxins requires extensive redox modifications of the phenalenone aromatic polyketide. *J Am Chem Soc* 140:6991–6997. <https://doi.org/10.1021/jacs.8b03705>.

21. Guengerich FP, Kim DH. 1991. Enzymatic oxidation of ethyl carbamate to vinyl carbamate and its role as an intermediate in the formation of 1,N6-ethenoadenosine. *Chem Res Toxicol* 4:413–421. <https://doi.org/10.1021/tx00022a003>.
22. Zhang X, Li S. 2017. Expansion of chemical space for natural products by uncommon P450 reactions. *Nat Prod Rep* 34:1061–1089. <https://doi.org/10.1039/c7np00028f>.
23. Pandey B, Ansari A, Vyas N, Rajaraman G. 2015. Structures, bonding and reactivity of iron and manganese high-valent metal-oxo complexes: a computational investigation. *J Chem Sci* 127:343–352. <https://doi.org/10.1007/s12039-015-0770-9>.
24. Lacy DC, Gupta R, Stone KL, Greaves J, Ziller JW, Hendrich MP, Borovik AS. 2010. Formation, structure, and EPR detection of a high spin FeIV—Oxo species derived from either an FeIII—Oxo or FeIII—OH complex. *J Am Chem Soc* 132:12188–12190. <https://doi.org/10.1021/ja1047818>.
25. Meunier B, de Visser SP, Shaik S. 2004. Mechanism of oxidation reactions catalyzed by cytochrome P450 enzymes. *Chem Rev* 104:3947–3980. <https://doi.org/10.1021/cr020443g>.
26. Bradford MM. 1976. A rapid and sensitive method for the quantitation of microgram quantities of protein utilizing the principle of protein-dye binding. *Anal Biochem* 72:248–254. <https://doi.org/10.1006/abio.1976.9999>.
27. Wang QS, Yu F, Huang S, Sun B, Zhang KH, Liu K, Wang ZJ, Xu CY, Wang SS, Yang LF, Pan QY, Li L, Zhou H, Cui Y, Xu Q, Earnest T, He JH. 2015. The macromolecular crystallography beamline of SSRF. *Nucl Sci Tech* 26:12–17. <https://doi.org/10.13538/j.1001-8042/nst.26.010102>.
28. Kabsch W. 2010. XDS. *Acta Crystallogr D Biol Crystallogr* 66:125–132. <https://doi.org/10.1107/S0907444909047337>.
29. Winn MD, Ballard CC, Cowtan KD, Dodson EJ, Emsley P, Evans PR, Keegan RM, Krissinel EB, Leslie AG, McCoy A, McNicholas SJ, Murshudov GN, Pannu NS, Potterton EA, Powell HR, Read RJ, Vagin A, Wilson KS. 2011. Overview of the CCP4 suite and current developments. *Acta Crystallogr D Biol Crystallogr* 67:235–242. <https://doi.org/10.1107/S0907444910045749>.
30. Adams PD, Afonine PV, Bunkoczi G, Chen VB, Davis IW, Echols N, Headd JJ, Hung LW, Kapral GJ, Grosse-Kunstleve RW, McCoy AJ, Moriarty NW, Oeffner R, Read RJ, Richardson DC, Richardson JS, Terwilliger TC, Zwart PH. 2010. PHENIX: a comprehensive Python-based system for macromolecular structure solution. *Acta Crystallogr D Biol Crystallogr* 66:213–221. <https://doi.org/10.1107/S0907444909052925>.
31. Emsley P, Lohkamp B, Scott WG, Cowtan K. 2010. Features and development of Coot. *Acta Crystallogr D Biol Crystallogr* 66:486–501. <https://doi.org/10.1107/S0907444910007493>.
32. Li S, Ouellet H, Sherman DH, Podust LM. 2009. Analysis of transient and catalytic desamine-binding pockets in cytochrome P-450 PikC from *Streptomyces venezuelae*. *J Biol Chem* 284:5723–5730. <https://doi.org/10.1074/jbc.M807592200>.
33. Abraham MJ, Murtola T, Schulz R, Páll S, Smith JC, Hess B, Lindahl E. 2015. GROMACS: high performance molecular simulations through multi-level parallelism from laptops to supercomputers. *SoftwareX* 1–2:19–25. <https://doi.org/10.1016/j.softx.2015.06.001>.
34. Søndergaard CR, Olsson MHM, Rostkowski M, Jensen JH. 2011. Improved treatment of ligands and coupling effects in empirical calculation and rationalization of pKa values. *J Chem Theory Comput* 7:2284–2295. <https://doi.org/10.1021/ct200133y>.
35. Schöneboom JC, Lin H, Reuter N, Thiel W, Cohen S, Ogliaro F, Shaik S. 2002. The elusive oxidant species of cytochrome P450 enzymes: characterization by combined quantum mechanical/molecular mechanical (QM/MM) calculations. *J Am Chem Soc* 124:8142–8151. <https://doi.org/10.1021/ja026279w>.
36. Parrinello M, Rahman A. 1981. Polymorphic transitions in single crystals: a new molecular dynamics method. *J Appl Phys* 52:7182–7182. <https://doi.org/10.1063/1.328693>.
37. Nosé S, Klein ML. 1983. Constant pressure molecular dynamics for molecular systems. *Mol Phys* 50:1055–1076. <https://doi.org/10.1080/00268978300102851>.
38. Evans DJ, Holian BL. 1985. The Nose-Hoover thermostat. *J Chem Phys* 83:4069–4074. <https://doi.org/10.1063/1.449071>.
39. Darden T, York D, Pedersen L. 1993. Particle mesh Ewald - an N-Log(N) method for Ewald sums in large systems. *J Chem Phys* 98:10089–10092. <https://doi.org/10.1063/1.464397>.
40. Essmann U, Perera L, Berkowitz ML, Darden T, Lee H, Pedersen LG. 1995. A smooth particle mesh Ewald method. *J Chem Phys* 103:8577–8593. <https://doi.org/10.1063/1.470117>.
41. Pall S, Hess B. 2013. A flexible algorithm for calculating pair interactions on SIMD architectures. *Comput Phys Commun* 184:2641–2650. <https://doi.org/10.1016/j.cpc.2013.06.003>.
42. Hess B, Bekker H, Berendsen HJC, Fraaije JGEM. 1997. LINCS: a linear constraint solver for molecular simulations. *J Comput Chem* 18:1463–1472. [https://doi.org/10.1002/\(SICI\)1096-987X\(199709\)18:12<1463::AID-JCC4>3.0.CO;2-H](https://doi.org/10.1002/(SICI)1096-987X(199709)18:12<1463::AID-JCC4>3.0.CO;2-H).
43. Miyamoto S, Kollman PA. 1992. Settle: an analytical version of the SHAKE and RATTLE algorithm for rigid water models. *J Comput Chem* 13:952–962. <https://doi.org/10.1002/jcc.540130805>.